Electronic Supplementary Material (ESI) for Journal of Materials Chemistry A.

Supporting Information: Probing catalytic surface by correlative scanning photoemission electron microscopy and atom probe tomography

Kevin Schweinar,*[a] Rachel L. Nicholls,[b] Catherine R. Rajamathi,[b] Patrick Zeller,[c] Matteo Amati,[c] Luca Gregoratti,[c] Dierk Raabe,[a] Mark Greiner,[b] Baptiste Gault,[a,d] and Olga Kasian[e,f]

[a.] Max-Planck-Institut für Eisenforschung GmbH, Microstructure Physics and Alloy Design, Düsseldorf, Germany

[b.] Max-Planck-Institut für Chemische Energiekonversion, Heterogeneous Reactions, Mülheim a.d. Ruhr, Germany

[c.] Elettra – Sincrotrone Trieste S.C.p.A., Trieste, Italy

[d.] Department of Materials, Imperial College London, Royal School of Mines, London, SW7 2AZ, UK

[e.] Max-Planck-Institut für Eisenforschung GmbH, Interface Chemistry and Surface Engineering, Düsseldorf, Germany

[f.] Helmholtz-Zentrum Berlin GmbH, Helmholtz-Institute Erlangen-Nürnberg, 14109 Berlin, Germany

*corresponding author: k.schweinar@mpie.de

Supplementary note to Figure S1

Care must be taken when interpreting SPEM data of beam sensitive materials such as oxides. Firstly, the exposure of a surface to the beam can result in the deposition of carbon species. Accumulation of carbon on the surface reduces the net signal of the elements of interest and potential binding energy overlaps, e.g. C 1s and Ru 3d in the present case, complicate the analysis of the collected spectra. Secondly, the high photon density used in SPEM involves a high risk of inducing damage to the surface. Particularly oxides are prone to reduce under the influence of the beam. The intensity of the incident synchrotron X-ray beam is further increased by approx. five orders of magnitude using the focusing optics to achieve a small spot size. Figure S1a and S1b show the comparison of the Ir 4f core level spectrum extracted from spectro-imaging (line with circles) and a spectrum collected in the µ-spot XPS mode (line). While the metallic spectra collected in the two different modes are consistent, one can observe a second shoulder in the oxide spectrum measured in the µ-spot XPS mode, which is not observed in the spectrum extracted from an image (indicated with an arrow). This shoulder exhibits a binding energy of 60.9 eV, consistent with an Ir^0 oxidation state. The longer exposure time of the probed region to the beam in the µ-spot XPS mode (300 ms per energy step) as compared to the spectro-imaging mode (30 ms per pixel) is the reason for the observation of a metallic contribution in the oxide spectrum. To clarify whether this spectrum represents a coexistence of Ir^0 and Ir^{IV} in the probed region or beam-induced reduction of Ir^{IV} to Ir^0, we decreased the dwell time per energy step to a minimum (30 ms) and collected a total of 80 "fast" sweeps, shown in Fig. S1C. The inspection of the spectra stack reveals (I) that the metallic contribution to the spectrum is already present during the first sweep and (II) that this contribution increases in intensity with the number of sweeps. We therefore interpret this as beam-induced reduction of the surface oxide.

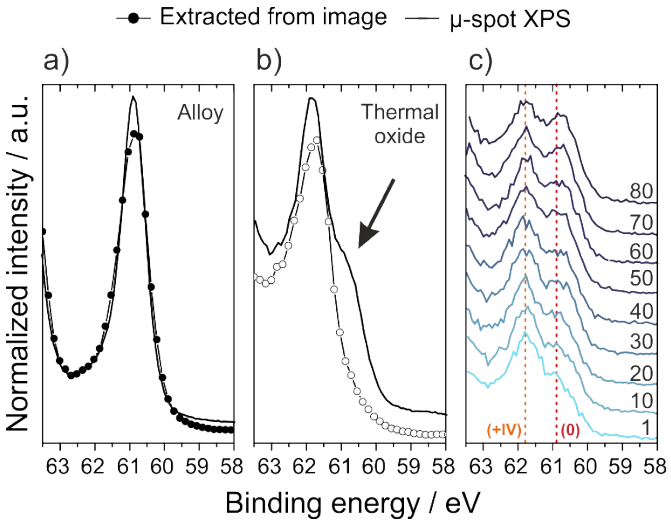

Figure S1. Beam damage analysis in spectra measured in XPS µ-spot mode. a) The spectra measured on the metallic alloy, b) the spectra obtained from a thermally oxidized sample, c) "fast" sweeps on thermal oxide

Supplementary note to Figure S2

Note that when ions are field evaporated during the APT measurement, they can not only evaporate as atomic ions in different charge states, e.g. Ir^{+}, Ir^{2+}, Ir^{3+}, or O^{+}, and O^{2+}, but they can also form molecular ions including e.g. IrO^{+}, IrO^{2+}, IrO_2^{+}, RuO_2^{2+}. The formation of molecular ions is particularly likely in oxides.[1] In the APT visualizations in Fig. 4, S2 and S4 we also present the detected molecular ionic species of IrO_x and RuO_x to improve the qualitative understanding of the distribution of different oxide species. Furthermore, the evaporation of CrO_x molecular ions close to the Cr/Ir-Ru(-oxide) interface complicates the oxygen quantification close to the material's surface, resulting in a larger experimental uncertainty in this region.

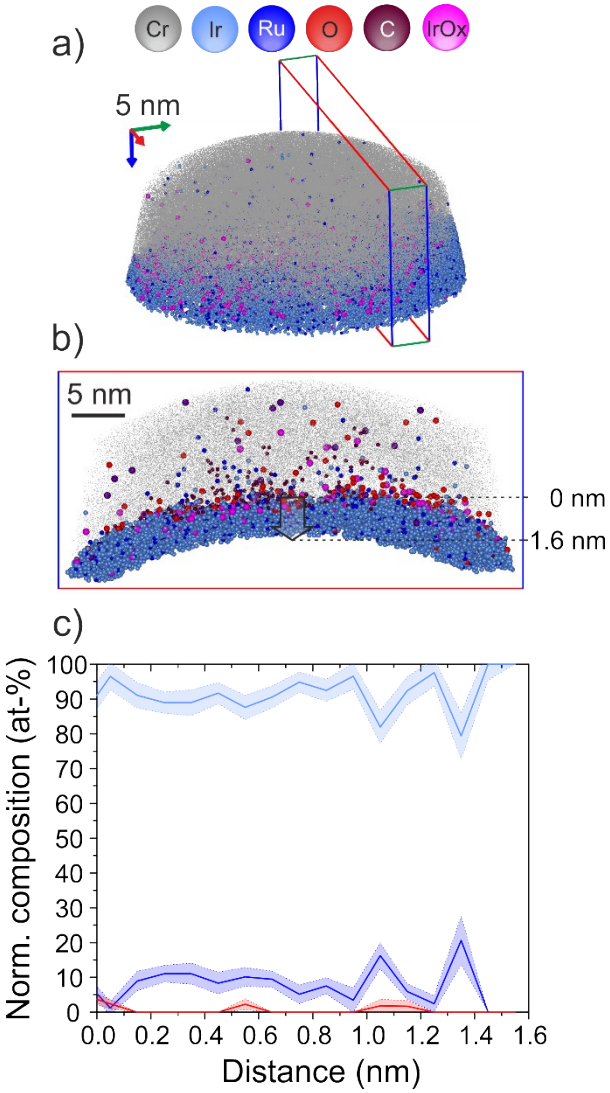

Figure S2. Atom probe tomography results of the as-deposited IrRu alloy. a) 3D reconstruction of evaporated volume. The coloured box indicates the location of the 5 nm thick extracted slice shown in a cross-sectional view in b). The cross-section reveals the presence of oxygen and carbon species on the surface of the specimen (i.e. at interface between Cr and Ir-Ru). These species are introduced by air and X-ray beam exposure of the sample during transport and the SPEM measurement. c) Composition profile along arrow shown in b). Profile starts at 0 nm distance, representing the physical surface of the sample identified by means of the first occurrence of adsorbed C species (not shown). The average composition of the initial alloy is $Ir_{0.92}Ru_{0.08}$, corresponding to an Ir-to-Ru ratio of 11.3.

Supplementary note to Figure S3

The center grain (II), shown in Fig. 4c, develops a stoichiometric oxide that becomes slightly richer in oxygen towards the surface, while maintaining the relative Ir-to-Ru ratio (Fig. S3e). The composition of this oxide is very close to the initial alloy ($Ir_{0.92}Ru_{0.08}$), also agreeing with limited diffusion of Ir and Ru. The observed increase in oxygen content towards the surface is likely caused by the increased quantification uncertainty related to the evaporation of CrO_x molecular ions close the the Cr/Ir-Ru-oxide interface (as mentioned in section 3.2.). However, an additional oxygen content contribution from adsorbed oxygen related to surface carbon or the formation of hydroxyl groups in the near-surface region is conceivable. The presence of additional O species in the near-surface region is supported by the O 1s spectrum, presented in Fig. 2c. Several O species at binding higher binding energies than the oxide lattice oxygen (529.8 eV) contribute to the experimental spectrum. It should be noted, though, that laser-assisted APT usually tends to underestimate the nominal oxygen content of oxides, [2-5] but rarely overestimates it. Regarding the origin of the additionally detected oxygen, the O 1s spectrum presented in Fig. 2c supports our interpretation, as several oxygen species at higher binding energies than the oxide lattice oxygen (529.8 eV) contribute to the experimental spectrum. Spectroscopy further suggests (+IV) metal ion oxidation states in this area on the surface, yet minor contributions of higher oxidation states might be present, but not detected due the lack of sensitivity of the measured Ir 4f and Ru 3d binding energies.

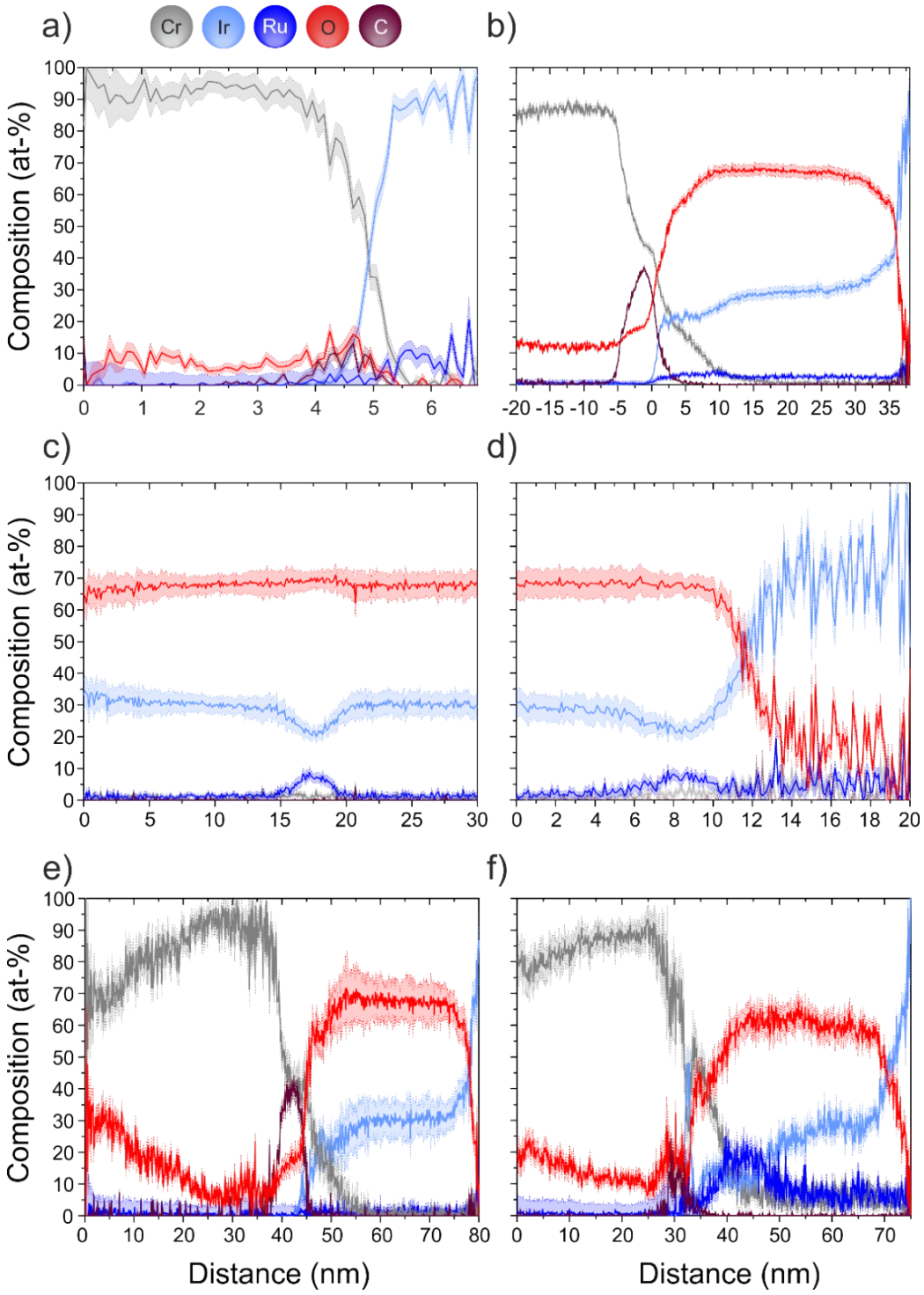

Figure S3. Full composition profiles including Cr and C. The occurrence of the latter was used to determine the actual top surface of the sample (interface Cr/Ir-Ru). a) as-deposited alloy. b) Proxigram of thermal oxide. c) – f) are profiles 1 – 4 (Fig. 4e,f,h,i) in the manuscript main text.

Supplementary note to Figure S4

Oxidized and non-oxidized grains seen in the APT data of the oxidized sample are a consequence of different crystal growth rates depending on the crystallographic orientation. There are reports of atomic scale evidence that IrO_2 can nucleate on different metal substrate facets.[6] The authors point out that the heating rate during the thermal oxidation process is a critical factor in the determination of which facets will be developed and eventually cover the surface. As the temperature is risen in an oxidative atmosphere, the first oxide nucleus is formed on the facet with the lowest energy barrier for nucleation – the (102) facet for the Ir-IrO_2 interface. If the temperature is then raised rapidly, further oxide nucleation on different facets will occur. If the temperature is raised slowly, the first nuclei may have time to grow until they cover the entire surface.[6] In view of the catalytic properties of the final product of the mixed oxide synthesis, this offers a further opportunity to tune the catalyst's properties by optimizing the oxidation process parameters

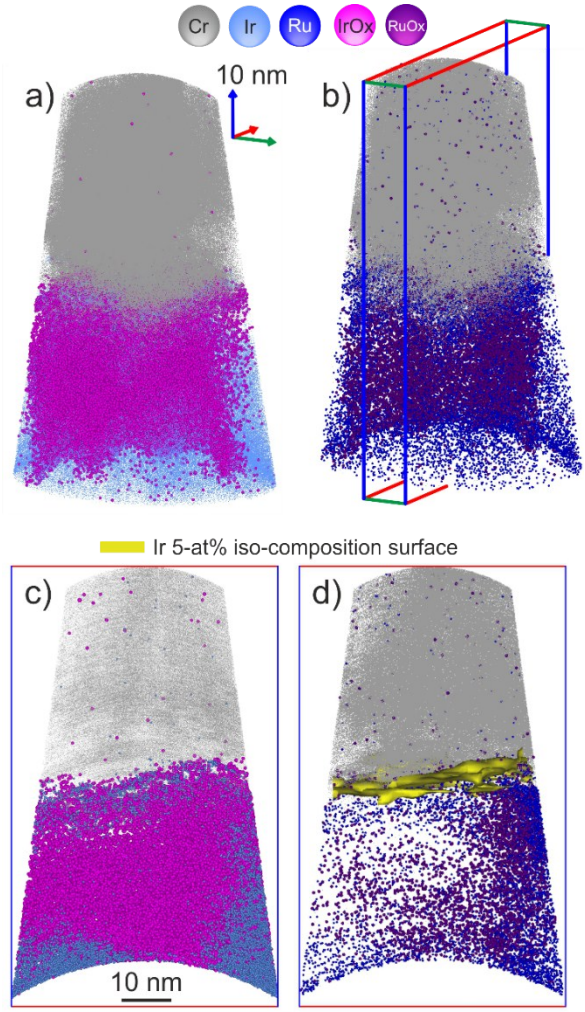

Figure S4. Atom probe reconstructions of the thermally oxidized sample. a) and b) show the reconstructed volumes in 3D. The images reveal that the measured volume comprises several grains that exhibit different oxygen contents (see main text). IrO_x and RuO_x species are heterogeneously distributed. c) and d) show a cross-sectional view on the box indicated in b). c) shows that center grain is strongly oxidized and rich in IrO_x, whereas Ru and RuO_x species are mainly concentrated along the grain boundary between the center grain and the grain on the right-hand side. The 5 at-% iso-composition surface shown in d) marks the surface from which a proxigram was calculated.

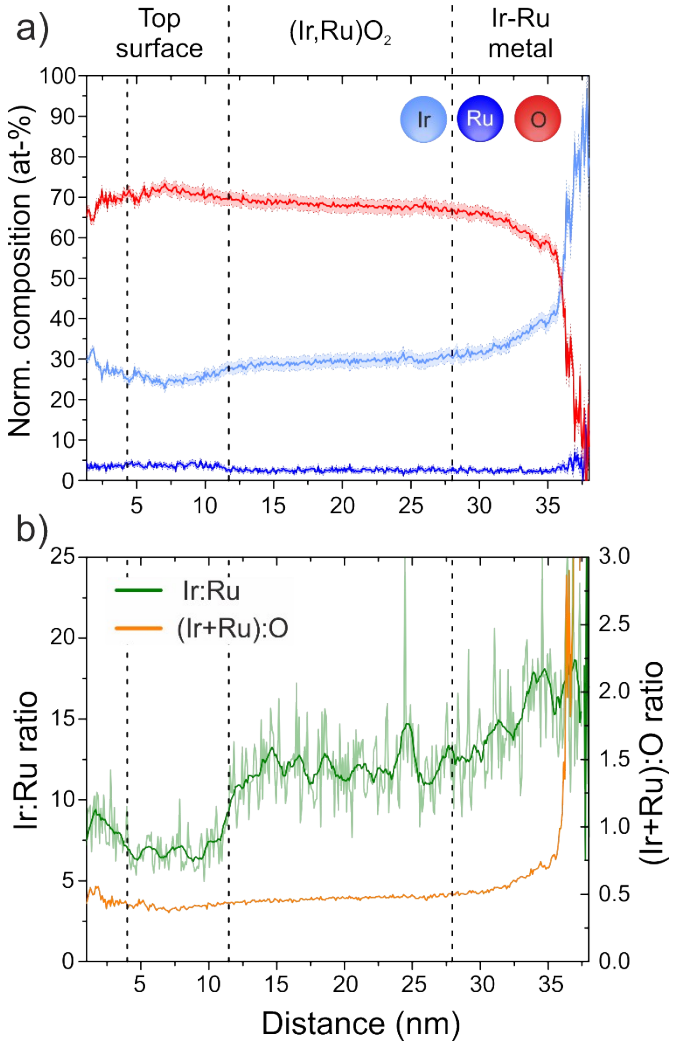

Figure S5. Composition analysis of APT data on thermal oxide. a) Proxigram calculated from a 5 at-% Ir iso-composition surface, as indicated in Fig. S3d. Proxigram provides a compositional analysis integrated over the entire field of view of the measurement (i.e. entire volume adjacent to iso-composition surface). b) Ir-to-Ru and (Ir+Ru)-to-O ratio calculated from the proxigram shown in a). The latter represents the local oxide stoichiometry.

Table S1. Normalized average compositions from the as-prepared sample. Note the strongly varying compositions along the grain boundaries of the material after sputter deposition.

	Normalized composition (at-%)
Average composition (proxigram) Top surface	$Ir_{0.92}Ru_{0.08}$
Local composition Grain composition	$Ir_{0.92}Ru_{0.08}$
Grain boundary composition	Fluctuating from $Ir_{0.81}Ru_{0.19}$ to $Ir_{0.55}Ru_{0.45}$

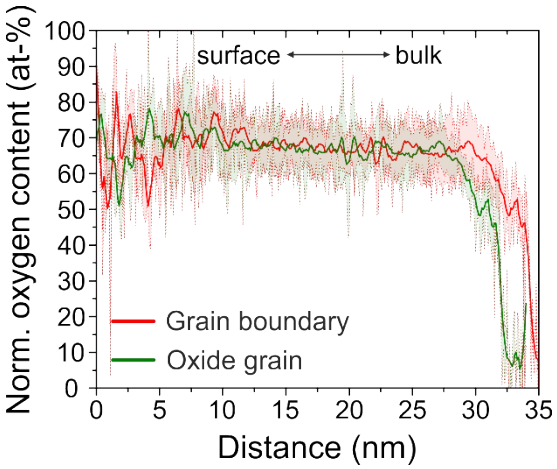

Figure S6. Oxygen depth profile along the grain boundary (red) and the adjacent bulk oxide grain (green) shown in Fig. 4c + d. The profiles reveal that the oxygen front has progressed deeper into the material along the grain boundary.

Supplementary note to Table S2

When comparing results from SPEM and APT, we consider only data from the volume of the sample that is accessible to both techniques. Further, we only consider averaged APT values (proxigram analysis) in the comparison, given the spatial resolution limits given by SPEM. The common volume is given by the probing depth of the SPEM measurements which we estimate to be <1.5 nm in the current experiments (hv = 650 eV, probing depth ~ 3 times inelastic mean free path (IMFP) of photoelectrons).

Table S2 Calculated inelastic mean free pathways (IMFP) according to the TPP-2M model[7] and for the experimentally used photon energy of hv = 650 eV. All IMPF are given in Å. The densities for the alloys and mixed oxides were obtained by averaging the densities of pure metals/oxides.

		Ru metal	Ir metal	Ir92Ru8	IrO2	RuO2	Ir0.92Ru0.08O2	Ir0.4Ru0.6O2
Density [g/cm^3]		12.37	22.56	21.74	11.7	6.97	11.46	9.59
VB electrons		8	23	21.8	35	20	33.8	26
Molar Mass [g/mol]		101.07	192.2	184.91	224.2	133.07	216.91	169.5
Signal	KE							
Ir 4f	589	**-**	**5.76**	**5.99**	**9.01**	**-**	**9.13**	**10.14**
Ru 3d	370	**7.24**	**-**	**4.36**	**-**	**8.61**	**6.67**	**7.44**
O 1s	120	**-**	**-**	**-**	**3.56**	**4.95**	**3.63**	**4.2**

References

1. Miller, M. K.; Forbes, R. G., Data Reconstruction. In *Atom-Probe Tomography: The Local Electrode Atom Probe*, Springer US: Boston, MA, 2014; pp 259-302.
2. Bachhav, M.; Danoix, F.; Hannoyer, B.; Bassat, J. M.; Danoix, R., Investigation of O-18 enriched hematite (α-Fe2O3) by laser assisted atom probe tomography. *International Journal of Mass Spectrometry* **2013,** *335*, 57-60.
3. Bachhav, M.; Danoix, R.; Danoix, F.; Hannoyer, B.; Ogale, S.; Vurpillot, F., Investigation of wüstite (Fe1−xO) by femtosecond laser assisted atom probe tomography. *Ultramicroscopy* **2011,** *111* (6), 584-588.
4. Kinno, T.; Tomita, M.; Ohkubo, T.; Takeno, S.; Hono, K., Laser-assisted atom probe tomography of 18O-enriched oxide thin film for quantitative analysis of oxygen. *Applied Surface Science* **2014,** *290*, 194-198.
5. La Fontaine, A.; Gault, B.; Breen, A.; Stephenson, L.; Ceguerra, A. V.; Yang, L.; Nguyen, T. D.; Zhang, J.; Young, D. J.; Cairney, J. M., Interpreting atom probe data from chromium oxide scales. *Ultramicroscopy* **2015,** *159 Pt 2*, 354-9.
6. Fortes, M. A.; Ralph, B.; Cottrell, A. H., The growth of oxide on field-ion specimens of iridium. *Proceedings of the Royal Society of London. Series A. Mathematical and Physical Sciences* **1968,** *307* (1491), 431-448.
7. Tanuma, S.; Powell, C. J.; Penn, D. R., Calculation of electron inelastic mean free paths (IMFPs) VII. Reliability of the TPP-2M IMFP predictive equation. *Surface and Interface Analysis* **2003,** *35* (3), 268-275.